Continuous full order model of triple active bridge converter

Purgát, Pavel; Bandyopadhyay, Soumya; Qin, Zian; Bauer, Pavol

DOI
10.23919/EPE.2019.8914897

Publication date
2019

Document Version
Final published version

Published in
2019 21st European Conference on Power Electronics and Applications (EPE '19 ECCE Europe)

Continuous Full Order Model of Triple Active Bridge Converter

Pavel Purgat, Soumya Bandyopadhyay, Zian Qin, Pavol Bauer
Electrical Sustainable Energy Department
TU Delft
Delft, Netherlands
Corresponding Author: p.purgat@tudelft.nl

Acknowledgments

This project has received funding in the framework of the joint programming initiative ERA-Net Smart Grids Plus, with support from the European Unions Horizon 2020 research and innovation programme.

Keywords

≪control≫, ≪dc-dc≫, ≪modelling≫.

Abstract

With the rising popularity of the power electronic based systems with integrated energy storage, the multi-port isolated converter topologies are gaining popularity. In contemporary literature, the triple active bridge (TAB) converter is the most popular among these topologies. However, the TAB was not yet described with the continuous-time full-order model. In this paper, the continuous-time full-order model of the TAB converter is derived. The derived model is validated with the measurement of the control-to-output transfer functions. The derived model can provide useful insights into the operation of the converter and can be used for controller design.

1 Introduction

The dawn of storage in the electric energy distribution brought increased interest in the multiport topologies with galvanic isolation. Among the topologies providing galvanic isolation, those based on phase-shift control such as dual active bridge (DAB) are in the centre of researchers attention. The main advantages of these topologies are the convenience of bi-directional power transfer and their ability to operate in soft switching mode across broad operating range [1], [2].

The triple active bridge (TAB) was for the first time introduced in [3] and [4]. The potential applications of the TAB converter include electric vehicles [5] and dc smart grids [6], [7]. The developments in dc-dc TAB include decoupling control [1], modelling [8], improving the soft-switching performance [9], and losses estimation [10].

Averaged models can be obtained via an averaged switch, averaged inductor current or averaged state-space model. If the converter violates the small-signal ripple condition such as TAB, one needs to resort to reduced-order models neglecting the current dynamics such as [11] or full-order discrete-time models such as [8]. However, to gain insights into the control and stability of the converter, it is often desirable to have continuous-time full-order models [12]. The main advantage of the continuous-time full-order models compared to the reduced order models is the increased accuracy [12].

The main contribution of this paper is the derivation of the continuous-time full-order model of a triple active bridge converter. The derived models are validated with the measurement of the transfer functions.

The rest of the paper is organized as follows. Section 2 describes the topology and explains the operating principles of the TAB. Section 3 presents the generalized averaging method, which is used to derive large

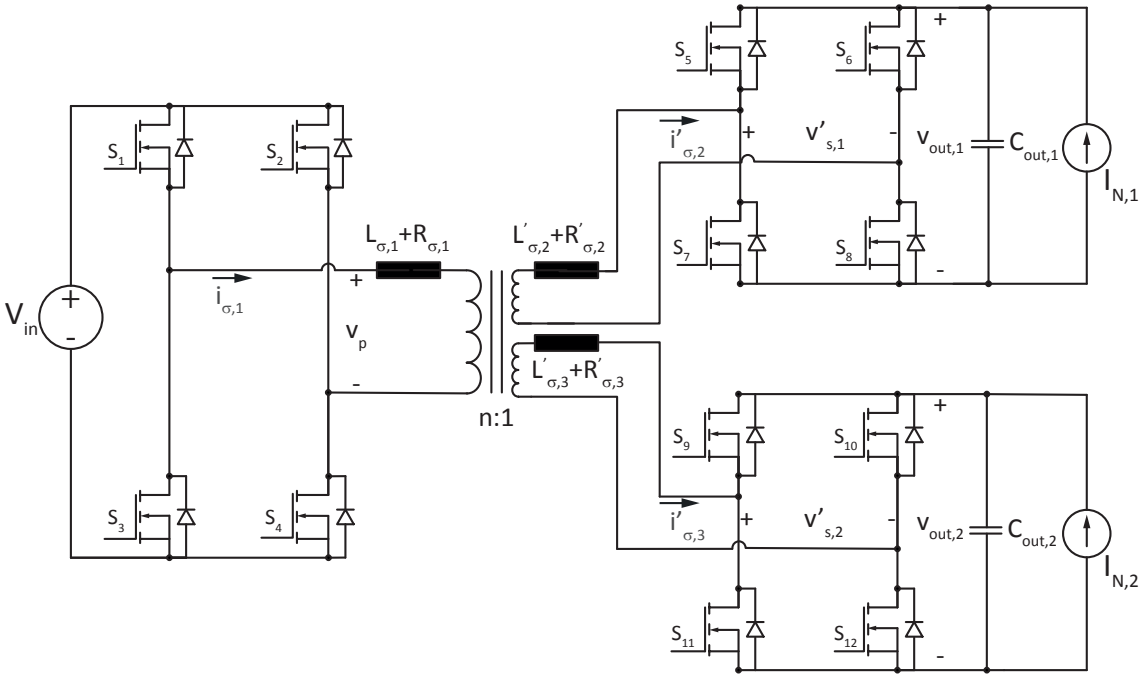

Fig. 1: Triple Active Bridge consits of 3 full bridges connected to a transformer with 3 windings.

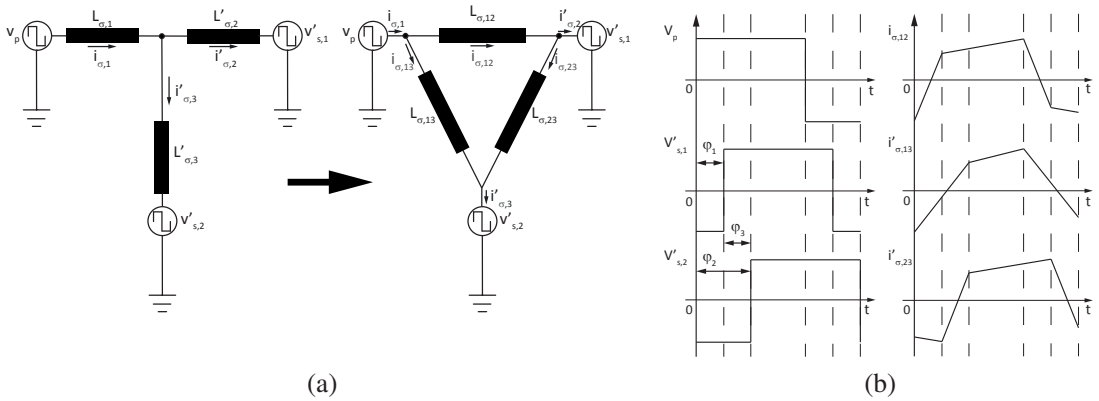

Fig. 2: Simplified schematic of the TAB converter before and after transformation is in (a), the theoretical operating waveforms of the converter are in (b).

and small-signal models of the TAB. Section 4 demonstrates the operation of the converter and validates the derived models with simulation and measurement of the control-to-output transfer functions. Section 5 summarizes the paper and gives an outlook on possible uses of the derived models.

2 Triple Active Bridge

The schematic of the TAB converter is in Fig. 1. The converter consists of three full bridges connected to the transformer with three windings. The power is transferred across the leakage inductances that can be inserted as separate components, or the transformer leakage inductances can be used. The zero voltage switching (ZVS) is achieved utilizing the parasitic capacitance of full bridges MOSFETs.

There are three options to control the TAB. First, is the phase-shift φ_x control between the full bridges, second is the control of duty ratios of the full bridges and third is the control of the switching frequency. In this work, only the phase shift control will be analyzed. For the phase-shift control, the duty cycle on

the full bridges is kept at 50%, and the power transfer is controlled by the phase shifts between the full bridges. In order to analyze the power transfer between the full bridges, it is beneficial to convert the schematic in Fig. 1 into a delta equivalent circuit.

Transformation

The Y-type equivalent circuit can be transformed into a delta type equivalent circuit as is depicted in Fig. 2b. The leakage inductances after the transformation are described as

$$\begin{aligned} L_{\sigma,12} &= L_{\sigma,1} + n^2 L_{\sigma,2} + \frac{L_{\sigma,1} L_{\sigma,2}}{L_{\sigma,3}}, \\ L_{\sigma,13} &= L_{\sigma,1} + n^2 L_{\sigma,3} + \frac{L_{\sigma,1} L_{\sigma,3}}{L_{\sigma,2}}, \\ L_{\sigma,32} &= n^2 L_{\sigma,3} + n^2 L_{\sigma,2} + n^4 \frac{L_{\sigma,3} L_{\sigma,2}}{L_{\sigma,1}}, \end{aligned} \tag{1}$$

where n is the transformer ratio and $L_{\sigma,1}$, $L_{\sigma,2}$ and $L_{\sigma,3}$ are the converter leakage inductances. The transformer currents in the converter after transformation are

$$\begin{aligned} i_{\sigma,1} &= -i_{\sigma,12} - i_{\sigma,13}, \\ i'_{\sigma,2} &= i_{\sigma,12} - i_{\sigma,23}, \\ i'_{\sigma,3} &= i_{\sigma,13} + i_{\sigma,23}, \end{aligned} \tag{2}$$

where $i_{\sigma,1}$ is the primary side transformer current and $i'_{\sigma,2}$ and $i'_{\sigma,3}$ are the secondary side transformer currents. The transformer ratio is accounted as $i'_{\sigma,2} = n i_{\sigma,2}$ and $i'_{\sigma,3} = n i_{\sigma,3}$.

Operation

When using the phase-shift modulation the voltage on the primary $v_p(\tau) = s_1(\tau) v_{in}(\tau)$ is achieved through the switching action which is defined as

$$s_1(\tau) = \begin{cases} 1 & \text{in} \quad 0 \le \tau < \frac{T_s}{2}, \\ -1 & \text{in} \quad \frac{T_s}{2} \le \tau < T_s, \end{cases} \tag{3}$$

where T_s is the switching period.

On the second port the voltage is $v'_{s,1}(\tau) = s_2(\tau) n v_{\text{out},1}(\tau)$ which is achieved via switching action

$$s_2(\tau) = \begin{cases} 1 & \text{in} \quad \frac{\varphi_1 T_s}{2} \le \tau < \frac{T_s}{2} + \frac{\varphi_1 T_s}{2}, \\ -1 & \text{in} \quad 0 \le \tau < \frac{\varphi_1 T_s}{2} \quad \text{and} \quad \frac{T_s}{2} + \frac{\varphi_1 T_s}{2} \le \tau < T_s, \end{cases} \tag{4}$$

where φ_1 is the phase-shift between voltage $v_p(\tau)$ and $v'_{s,1}(\tau)$.

And on the third port the voltage is $v'_{s,2}(\tau) = s_3(\tau) n v_{\text{out},2}(\tau)$ obtained via switching action

$$s_3(\tau) = \begin{cases} 1 & \text{in} \quad \frac{\varphi_2 T_s}{2} \le \tau < \frac{T_s}{2} + \frac{\varphi_2 T_s}{2}, \\ -1 & \text{in} \quad 0 \le \tau < \frac{\varphi_2 T_s}{2} \quad \text{and} \quad \frac{T_s}{2} + \frac{\varphi_2 T_s}{2} \le \tau < T_s, \end{cases} \tag{5}$$

where φ_2 is the phase-shift between voltage $v_p(\tau)$ and $v'_{s,2}(\tau)$.

The equations describing operation of the TAB converter depicted on Fig.1 after transformation of the

lekeage inductor currents are

$$C_{\text{out},1}\frac{\mathrm{d}}{\mathrm{d}\tau}v_{\text{out},1}(\tau) = -\frac{v_{\text{out},1}(\tau)}{R_{\text{out},1}} + s_2(\tau)i'_{\sigma,2}(\tau) + I_{N,1}, \tag{6}$$

$$C_{\text{out},2}\frac{\mathrm{d}}{\mathrm{d}\tau}v_{\text{out},2}(\tau) = -\frac{v_{\text{out},2}(\tau)}{R_{\text{out},2}} + s_3(\tau)i'_{\sigma,3}(\tau) + I_{N,2}, \tag{7}$$

$$L_{\sigma,12}\frac{\mathrm{d}}{\mathrm{d}\tau}i_{\sigma,12}(\tau) = -R_{\sigma,12}i_{\sigma,12}(\tau) + v_p(\tau) - v'_{s,1}(\tau), \tag{8}$$

$$L_{\sigma,13}\frac{\mathrm{d}}{\mathrm{d}\tau}i_{\sigma,13}(\tau) = -R_{\sigma,13}i_{\sigma,13}(\tau) + v_p(\tau) - v'_{s,2}(\tau), \tag{9}$$

$$L_{\sigma,23}\frac{\mathrm{d}}{\mathrm{d}\tau}i_{\sigma,23}(\tau) = -R_{\sigma,23}i_{\sigma,23}(\tau) + v'_{s,1}(\tau) - v'_{s,2}(\tau), \tag{10}$$

where $C_{\text{out},1}$, $C_{\text{out},2}$ are the output capacitances, $R_{\text{out},1}$ and $R_{\text{out},2}$ are the output resistances, $I_{N,1}$ and $I_{N,2}$ are the output dc currents and $R_{\sigma,12}$, $R_{\sigma,13}$ and $R_{\sigma,23}$ are the parasitic resistances in the delta type equivalent circuit of the TAB.

In eq. (6)-(10) it is assumed that transformer magnetization current is insignificant. Further, the MOSFET switching transients are neglected as well as the voltage drop across the MOSFET body diode. The polarity of the output current sources $I_{N,1}$ and $I_{N,2}$ can be both positive and negative to allow the bi-directional power transfer. The input capacitance is coupled in the ideal voltage source V_{in}, and the reason is twofold. First, the input capacitance is normally large enough to minimize any ripple. Secondly in most cases it is desired to control the voltages on the secondary side of the converter, therefore output capacitors $C_{\text{out},1}$ and $C_{\text{out},2}$ are modelled. The parasitic resistances $R_{\sigma,12}$, $R_{\sigma,13}$ and $R_{\sigma,23}$ represent both the ohmic losses in the magnetic circuit as well as in the semiconductors.

3 Modelling

Generalized Averaging Method

The generalized averaging method was derived in [13], motivated by the switching circuits that did not fulfil the small-ripple condition. The generalized averaging method was applied to the DAB in [12]. Recently it was improved to limit the small steady-state error in the closed-loop control signal of the DAB in [14] and even reformulated for the use with dc grid models in [15].

Because in the case of the TAB, the ac ripple in the current is far from being negligible, the generalized averaging method needs to be applied. The core idea is to represent the state-space variable during the switching interval $t - T_s \leq \tau < t$ using Fourier series approximation

$$x(\tau) = \sum_{k=-\infty}^{\infty} \langle x\rangle_k(t)e^{-jk\omega_s\tau}, \tag{11}$$

where $\langle x\rangle_k$ is the $k-th$ coefficient of the Fourier series and can be expressed as

$$\begin{aligned}\langle x\rangle_k(t) &= \frac{1}{T}\int_{t-T+s}^{t} x(\tau)e^{-jk\omega_s\tau}\mathrm{d}\tau \\ &= \frac{1}{T}\int_{t-T+s}^{t} x(\tau)\cos(k\omega_s\tau)\mathrm{d}\tau \\ &- \frac{j}{T}\int_{t-T+s}^{t} x(\tau)\sin(k\omega_s\tau)\mathrm{d}\tau.\end{aligned} \tag{12}$$

The switching coefficients when the duty ratio is fixed to 50% after averaging are

$$\langle s_1\rangle_0 = \langle s_1\rangle_{1R} = \langle s_2\rangle_0 = \langle s_3\rangle_0 = 0, \tag{13}$$

and

$$\langle s_1\rangle_{1I} = -\frac{2}{\pi}, \tag{14}$$
$$\langle s_2\rangle_{1R} = -\frac{2\sin(d_1\pi)}{\pi}, \tag{15}$$
$$\langle s_2\rangle_{1I} = -\frac{2\cos(d_1\pi)}{\pi}, \tag{16}$$
$$\langle s_3\rangle_{1R} = -\frac{2\sin(d_2\pi)}{\pi}, \tag{17}$$
$$\langle s_3\rangle_{1I} = -\frac{2\cos(d_2\pi)}{\pi}, \tag{18}$$

where d_1 and d_2 are the phase-shift ratios equal to $\frac{\varphi_1}{\pi}$ and $\frac{\varphi_2}{\pi}$ respectively.

The generalized averaging method will not be applied explicitly here to eq. (6)-(10) in order to keep the length of the paper reasonable. However, the generalized averaging method was explicitly applied to DAB equations in [12].

Large Signal Model

We can assume that the dynamics of the input voltage source and the output current sources are much slower than that of the TAB. Therefore the dynamics of the averaged input voltage source and output current sources fulfil following set of equations $\langle v_{\text{in}}\rangle_0 = V_{\text{in}}$, $\langle v_{\text{in}}\rangle_{1R} = \langle v_{\text{in}}\rangle_{1I} = 0$, $\langle i_{N,1}\rangle_0 = I_{N,1}$, $\langle i_{N,1}\rangle_{1R} = \langle i_{N,1}\rangle_{1I} = 0$, $\langle i_{N,2}\rangle_0 = I_{N,2}$, $\langle i_{N,2}\rangle_{1R} = \langle i_{N,2}\rangle_{1I} = 0$. The large-signal model of the TAB can be written in the state-space form as shown in eq. (19).

Small Signal Model

To derive the small-signal average model of the converter, we first define the small-signal deviations as $\Delta d_1 = d_1 - D_1, \Delta d_2 = d_2 - D_2, \Delta v_{\text{out},1} = v_{\text{out},1} - V_{\text{out},1}, \Delta v_{\text{out},2} = v_{\text{out},2} - V_{\text{out},2}, \Delta i_{\sigma,12R} = i_{\sigma,12R} - I_{\sigma,12R}, \Delta i_{\sigma,12I} = i_{\sigma,12I} - I_{\sigma,12I}, \Delta i_{\sigma,13R} = i_{\sigma,13R} - I_{\sigma,13R}, \Delta i_{\sigma,13I} = i_{\sigma,13I} - I_{\sigma,13I}, \Delta i_{\sigma,23R} = i_{\sigma,23R} - I_{\sigma,23R}, \Delta i_{\sigma,23I} = i_{\sigma,23I} - I_{\sigma,23I}$. where Δ defines the small-signal state, the upper case letters represent the dc terms and the lower case letters the large-signal states.

Equation (19) contains nonlinear terms such as multiplication of the control input and state variables.

$$\frac{\mathrm{d}}{\mathrm{d}t}\begin{bmatrix} v_{\text{out},1} \\ v_{\text{out},2} \\ i_{\sigma,12R} \\ i_{\sigma,12I} \\ i_{\sigma,13R} \\ i_{\sigma,13I} \\ i_{\sigma,23R} \\ i_{\sigma,23I} \end{bmatrix} = \begin{bmatrix} \frac{-1}{R_{\text{out},1}C_{\text{out},1}} & 0 & \frac{-4n\sin(d_1\pi)}{\pi C_{\text{out},1}} & \frac{-4n\cos(d_1\pi)}{\pi C_{\text{out},1}} & 0 & 0 & \frac{4n\sin(d_1\pi)}{\pi C_{\text{out},1}} & \frac{4n\cos(d_1\pi)}{\pi C_{\text{out},1}} \\ 0 & \frac{-1}{R_{\text{out},2}C_{\text{out},2}} & 0 & 0 & \frac{-4n\sin(d_2\pi)}{\pi C_{\text{out},2}} & \frac{-4n\cos(d_2\pi)}{\pi C_{\text{out},2}} & -\frac{4n\sin(d_2\pi)}{\pi C_{\text{out},2}} & -\frac{4n\cos(d_2\pi)}{\pi C_{\text{out},2}} \\ \frac{2n\sin(d\pi)}{\pi L_{\sigma,12}} & 0 & \frac{-R_\sigma}{L_{\sigma,12}} & \omega_s & 0 & 0 & 0 & 0 \\ \frac{2n\cos(d\pi)}{\pi L_{\sigma,12}} & 0 & -\omega_s & \frac{-R_\sigma}{L_{\sigma,12}} & 0 & 0 & 0 & 0 \\ 0 & \frac{2n\sin(d_2\pi)}{\pi L_{\sigma,13}} & 0 & 0 & \frac{-R_\sigma}{L_{\sigma,13}} & \omega_s & 0 & 0 \\ 0 & \frac{2n\cos(d_2\pi)}{\pi L_{\sigma,13}} & 0 & 0 & -\omega_s & \frac{-R_\sigma}{L_{\sigma,13}} & 0 & 0 \\ \frac{2n\sin(d_1\pi)}{\pi L_{\sigma,23}} & \frac{-2n\sin(d_2\pi)}{\pi L_{\sigma,23}} & 0 & 0 & 0 & 0 & \frac{-R_\sigma}{L_{\sigma,23}} & \omega_s \\ \frac{-2n\cos(d_1\pi)}{\pi L_{\sigma,23}} & \frac{2n\cos(d_2\pi)}{\pi L_{\sigma,23}} & 0 & 0 & 0 & 0 & -\omega_s & \frac{-R_\sigma}{L_{\sigma,23}} \end{bmatrix} \times \begin{bmatrix} v_{\text{out},1} \\ v_{\text{out},2} \\ i_{\sigma,12R} \\ i_{\sigma,12I} \\ i_{\sigma,13R} \\ i_{\sigma,13I} \\ i_{\sigma,23R} \\ i_{\sigma,23I} \end{bmatrix} + \begin{bmatrix} 0 & -\frac{1}{C_{\text{out},1}} & 0 \\ 0 & 0 & -\frac{1}{C_{\text{out},2}} \\ 0 & 0 & 0 \\ \frac{-2}{\pi L_{\sigma,12}} & 0 & 0 \\ 0 & 0 & 0 \\ \frac{-2}{\pi L_{\sigma,13}} & 0 & 0 \\ 0 & 0 & 0 \\ 0 & 0 & 0 \end{bmatrix} \begin{bmatrix} V_{\text{in}} \\ I_{N,1} \\ I_{N,2} \end{bmatrix}. \tag{19}$$

For small Δd_1, the nonlinear term can be written as

$$\sin(\pi d_1)v_{\text{out},1_0} = \sin(\pi D_1)\Delta v_{\text{out},1_0} + V_{\text{out},1_0}\sin(\pi D_1) + V_{\text{out},1_0}\cos(\pi D_1)(\pi D_1). \tag{20}$$

The small signal model of the TAB converter is written in eq. (21).

4 Simulation and Experiment

In order to verify the proposed model simulation and experimental results are compared. The small-signal models are verified via measurement of the control-to-output transfer function. The control-to-output transfer functions of the converter were measured with vector analyzer Bode 100, which operation is described in [16].

The TAB prototype is shown in Fig. 3, and the circuit parameters are summarized in Table I. During the measurements, the input voltage was 100 V, to keep the measuring probes of the vector analyzer Bode 100 safe. The load resistances $R_{\text{out},1}$ and $R_{\text{out},2}$ were set to 9 Ω and the converter switching frequency was 20 kHz. The converter prototype is controlled using microprocessor TMS320F28379D from Texas Instruments.

An example of the operating waveforms of the TAB prototype are in Fig.4. Figure 4a shows the waveforms of the converter when the phase-shifts φ_1 and φ_2 are the same, i.e. φ_3 is equal to zero. Figure 4b shows the waveforms of the converter when φ_1 and φ_2 are different. During this operation mode, there is power transferred between the two secondary ports because φ_3 is not equal to zero.

The magnitudes of the control-to-output transfer functions of the TAB are compared in Fig. 4c-4f. The solid line represents the simulated results, while the crosses represent the measured data points. The mismatch between the measurement and the simulation is minor. Further improvement in the accuracy could come from including higher order components of the Fourier series. Incorporating these terms would improve the precision in the higher frequency part of the Bode plots. Improvement in the low-frequency part of the Bode plot can be gained when improved GAM models are used such as [14]. However, the match between the measured results and the simulation give confidence that the derived model is valid. Moreover, the model in the present form gives good trade-off between complexity and accuracy and can be used to design novel controllers.

$$\frac{\mathrm{d}}{\mathrm{d}t}\begin{bmatrix}\Delta v_{\text{out},1}\\ \Delta v_{\text{out},2}\\ \Delta i_{\sigma,12R}\\ \Delta i_{\sigma,12I}\\ \Delta i_{\sigma,13R}\\ \Delta i_{\sigma,13I}\\ \Delta i_{\sigma,23R}\\ \Delta i_{\sigma,23I}\end{bmatrix} = \begin{bmatrix}
\frac{-1}{R_{\text{out},1}C_{\text{out},1}} & 0 & \frac{-4n\sin(D_1\pi)}{\pi C_{\text{out},1}} & \frac{-4n\cos(D_1\pi)}{\pi C_{\text{out},1}} & 0 & 0 & \frac{4n\sin(D_1\pi)}{\pi C_{\text{out},1}} & \frac{4n\cos(D_1\pi)}{\pi C_{\text{out},1}}\\
0 & \frac{-1}{R_{\text{out},2}C_{\text{out},2}} & 0 & 0 & \frac{-4n\sin(D_2\pi)}{\pi C_{\text{out},2}} & \frac{-4n\cos(D_2\pi)}{\pi C_{\text{out},2}} & \frac{4n\sin(D_2\pi)}{\pi C_{\text{out},2}} & \frac{4n\cos(D_2\pi)}{\pi C_{\text{out},2}}\\
\frac{2n\sin(D_1\pi)}{\pi L_{\sigma,12}} & 0 & \frac{-R_\sigma}{L_{\sigma,12}} & \omega_s & 0 & 0 & 0 & 0\\
\frac{2n\cos(D_1\pi)}{\pi L_{\sigma,12}} & 0 & -\omega_s & \frac{-R_\sigma}{L_{\sigma,12}} & 0 & 0 & 0 & 0\\
0 & \frac{2n\sin(D_2\pi)}{\pi L_{\sigma,13}} & 0 & 0 & \frac{-R_\sigma}{L_{\sigma,13}} & \omega_s & 0 & 0\\
0 & \frac{2n\cos(D_2\pi)}{\pi L_{\sigma,13}} & 0 & 0 & -\omega_s & \frac{-R_\sigma}{L_{\sigma,13}} & 0 & 0\\
\frac{2n\sin(D_1\pi)}{\pi L_{\sigma,23}} & \frac{-2n\sin(D_2\pi)}{\pi L_{\sigma,23}} & 0 & 0 & 0 & 0 & \frac{-R_\sigma}{L_{\sigma,23}} & \omega_s\\
\frac{-2n\cos(D_1\pi)}{\pi L_{\sigma,23}} & \frac{2n\cos(D_2\pi)}{\pi L_{\sigma,23}} & 0 & 0 & 0 & 0 & -\omega_s & \frac{-R_\sigma}{L_{\sigma,23}}
\end{bmatrix}
\times \begin{bmatrix}\Delta v_{\text{out},1}\\ \Delta v_{\text{out},2}\\ \Delta i_{\sigma,12R}\\ \Delta i_{\sigma,12I}\\ \Delta i_{\sigma,13R}\\ \Delta i_{\sigma,13I}\\ \Delta i_{\sigma,23R}\\ \Delta i_{\sigma,23I}\end{bmatrix} + \begin{bmatrix}
0 & -4n\left[I_{3R,0}\cos(\pi D_2)) - I_{3I,0}\sin(\pi D_2))\right]\\
2nV_{\text{out},1,0}\cos(\pi D_1) & 0\\
-2nV_{\text{out},1,0}\sin(\pi D_1) & 0\\
0 & 2nV_{\text{out},2,0}\cos(\pi D_2)\\
0 & -2nV_{\text{out},2,0}\sin(\pi D_2)\\
2nV_{\text{out},1,0}\cos(\pi D_1) & -2nV_{\text{out},2,0}\cos(\pi D_2)\\
-2nV_{\text{out},1,0}\sin(\pi D_1) & -2nV_{\text{out},2,0}\sin(\pi D_2)
\end{bmatrix}\begin{bmatrix}\Delta d_1\\ \Delta d_2\end{bmatrix}. \tag{21}$$

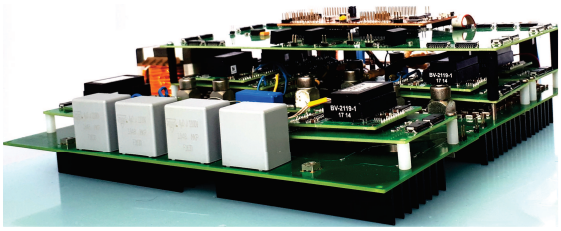

Fig. 3: The triple active bridge prototype.

Parameter	Acronym	Value
Transformer ratio	n	7 [-]
Primary Inductance	$L_{\sigma,1}$	78 [μH]
Secondary Inductance	$L_{\sigma,2\&3}$	15.5 [μH]
Output Capacitance	$C_{out,1\&2}$	1.22 [mF]
Primary Resistance	$R_{\sigma,1}$	20 [mΩ]
Secondary Resistance	$R_{\sigma,2\&3}$	.4 [mΩ]

Table I

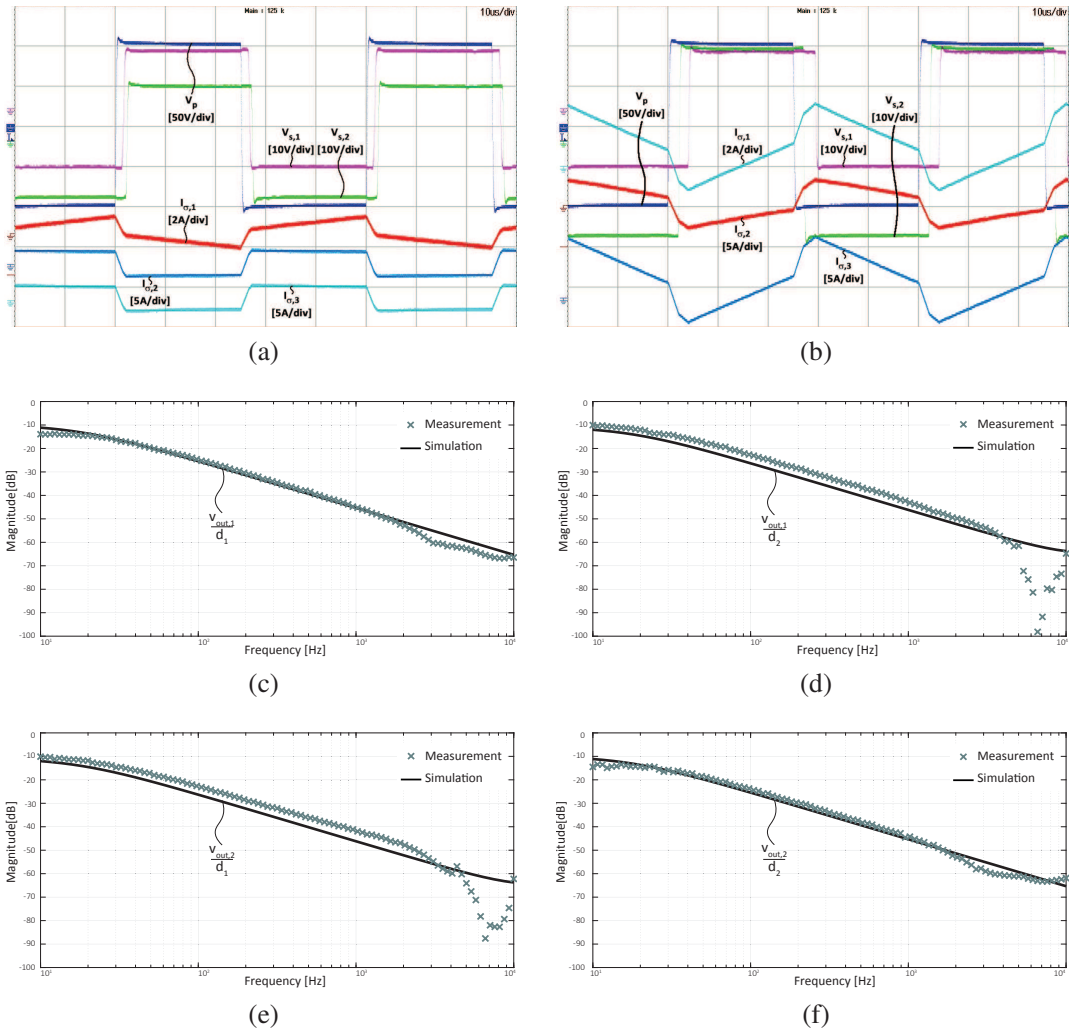

Fig. 4: Experimental and simulation results showcasing the operation of the prototype and validating the proposed model. In (a) is the operation of the converter when the phase-shift φ_3 is zero while in (b) φ_3 is non-zero. In (c), (d), (e), (f) are measured and simulated control-to-output transfer functions of the TAB.

The equivalent series resistance (ESR) of the output capacitors is not considered here. The effect of the ESR on the model performance was already described for DAB in [12]. Moreover, the current prototype employs extremely efficient capacitor bank based on the X7R technology, which minimizes the ESR virtually to zero, making the ESR effect almost unmeasurable.

5 Conclusion

The paper presented a continuous-time full-order model of the triple active bridge converter (TAB). The proposed model uses switching frequency terms in the Fourier series of the state variables and can describe the dynamics of the purely ac transformer currents. This feature is particularly important when working with TAB converters because it provides insights into the origin of the coupling between the state variables. The proposed model is validated via measurement of the control-to-output transfer functions of the TAB converter. The simulation and experimental results show that the proposed model is accurate. Moreover, the proposed model offers a good trade-off between complexity and accuracy. Therefore it can be used to design new control laws for the TAB.

References

[1] C. Zhao, S. D. Round, and J. W. Kolar, "An isolated three-port bidirectional dc-dc converter with decoupled power flow management," *IEEE Transactions on Power Electronics*, vol. 23, no. 5, pp. 2443–2453, Sept 2008.

[2] Z. Qin, Y. Shen, P. C. Loh, H. Wang, and F. Blaabjerg, "A dual active bridge converter with an extended high-efficiency range by dc blocking capacitor voltage control," *IEEE Transactions on Power Electronics*, vol. 33, no. 7, pp. 5949–5966, July 2018.

[3] Chuanhong Zhao and J. W. Kolar, "A novel three-phase three-port ups employing a single high-frequency isolation transformer," in *2004 IEEE 35th Annual Power Electronics Specialists Conference (IEEE Cat. No.04CH37551)*, vol. 6, June 2004, pp. 4135–4141 Vol.6.

[4] J. L. Duarte, M. Hendrix, and M. G. Simoes, "Three-port bidirectional converter for hybrid fuel cell systems," *IEEE Transactions on Power Electronics*, vol. 22, no. 2, pp. 480–487, March 2007.

[5] S. Y. Kim, H. Song, and K. Nam, "Idling port isolation control of three-port bidirectional converter for evs," *IEEE Transactions on Power Electronics*, vol. 27, no. 5, pp. 2495–2506, May 2012.

[6] M. Neubert, A. Gorodnichev, J. Gottschlich, and R. W. D. Doncker, "Performance Analysis of a Triple-Active Bridge Converter for Interconnection of Future DC-Grids," *2016 IEEE Energy Conversion Congress and Exposition (ECCE)*, pp. 1–8, 2016.

[7] P. Purgat, L. Mackay, M. Schulz, Y. Han, Z. Qin, M. Mrz, and P. Bauer, "Design of a power flow control converter for bipolar meshed lvdc distribution grids," in *2018 IEEE 18th International Power Electronics and Motion Control Conference (PEMC)*, Aug 2018, pp. 1073–1078.

[8] C. Zhao, S. D. Round, and J. W. Kolar, "Full-order averaging modelling of zero-voltage-switching phase-shift bidirectional dc-dc converters," *IET Power Electronics*, vol. 3, no. 3, pp. 400–410, May 2010.

[9] L. Jiang and D. Costinett, "A Triple Active Bridge DC-DC Converter Capable of Achieving Full-Range ZVS," *2016 IEEE Applied Power Electronics Conference and Exposition (APEC)*, vol. 3, no. c, pp. 872–879, 2016.

[10] L. Piris-Botalla, G. G. Oggier, A. M. Airabella, and G. O. Garca, "Analysis and evaluation of power switch losses for three-port bidirectional dc-dc converter," in *2012 IEEE International Conference on Industrial Technology*, March 2012, pp. 950–955.

[11] H. K. Krishnamurthy and R. Ayyanar, "Building block converter module for universal (ac-dc, dc-ac, dc-dc) fully modular power conversion architecture," in *2007 IEEE Power Electronics Specialists Conference*, June 2007, pp. 483–489.

[12] H. Qin and J. W. Kimball, "Generalized average modeling of dual active bridge dcdc converter," *IEEE Transactions on Power Electronics*, vol. 27, no. 4, pp. 2078–2084, April 2012.

[13] S. R. Sanders, J. M. Noworolski, X. Z. Liu, and G. C. Verghese, "Generalized averaging method for power conversion circuits," *IEEE Transactions on Power Electronics*, vol. 6, no. 2, pp. 251–259, April 1991.

[14] J. A. Mueller and J. W. Kimball, "An improved generalized average model of dcdc dual active bridge converters," *IEEE Transactions on Power Electronics*, vol. 33, no. 11, pp. 9975–9988, Nov 2018.

[15] J. A. Mueller and J. Kimball, "Modeling dual active bridge converters in dc distribution systems," *IEEE Transactions on Power Electronics*, pp. 1–1, 2018.

[16] S. Synkule, L. Heinzle, F. Hecht, and F. Hmmerle, *DC/DC Converter Stability Measurement*, OMICRON Lab, 2018.